

# Accuracy enhancement of the spherical actuator with a two-level geometric calibration method

Zhang, Liang; Chen, Weihai; Liu, Jingmeng; Wu, Xingming; Chen, I-Ming

2014

Zhang, L., Chen, W., Liu, J., Wu, X., & Chen, I.-M. (2014). Accuracy enhancement of the spherical actuator with a two-level geometric calibration method. Chinese journal of aeronautics, 27(2), 328-337.

<https://hdl.handle.net/10356/100185>

<https://doi.org/10.1016/j.cja.2014.02.001>

---

© 2014 Production and hosting by Elsevier Ltd. on behalf of CSAA & BUAA. Open access under CC BY-NC-ND license.

*Downloaded on 13 Mar 2024 16:58:29 SGT*



Chinese Society of Aeronautics and Astronautics  
& Beihang University

Chinese Journal of Aeronautics

cja@buaa.edu.cn  
www.sciencedirect.com



# Accuracy enhancement of the spherical actuator with a two-level geometric calibration method

Zhang Liang <sup>a</sup>, Chen Weihai <sup>a,\*</sup>, Liu Jingmeng <sup>a</sup>, Wu Xingming <sup>a</sup>, Chen I-Ming <sup>b</sup>

<sup>a</sup> School of Automation Science and Electrical Engineering, Beihang University, Beijing 100191, China

<sup>b</sup> School of Mechanical and Aerospace Engineering, Nanyang Technological University, 50 Nanyang Ave. 639798, Singapore

Received 3 April 2013; revised 14 June 2013; accepted 27 August 2013

Available online 19 February 2014

## KEYWORDS

Actuators;  
Geometric calibration;  
Parameter identification;  
Positioning accuracy;  
Spherical actuator

**Abstract** This paper presents a two-level geometric calibration method for the permanent magnet (PM) spherical actuator to improve its motion control accuracy. The proposed actuator is composed of a stator with circumferential coils and a rotor with multiple PM poles. Due to the assembly and fabrication errors, the real geometric parameters of the actuator will deviate from their design values. Hence, the identification of such errors is critical for the motion control tasks. A two-level geometric calibration approach is proposed to identify such errors. In the first level, the calibration model is formulated based on the differential form of the kinematic equation, which is to identify the geometric errors in the spherical joint. In the second level, the calibration model is formulated based on the differential form of torque formula, which is to calibrate the geometric parameters of the magnetization axes of PM poles and coils axes. To demonstrate the robustness and availability of the calibration algorithm, simulations are conducted. The results have shown that the proposed two-level calibration method can effectively compensate the geometric parameter errors and improve the positioning accuracy of the spherical actuator.

© 2014 Production and hosting by Elsevier Ltd. on behalf of CSAA & BUAA.

Open access under [CC BY-NC-ND license](#).

## 1. Introduction

Multi-degree-of-freedom (multi-DOF) spherical motion has wide application in aviation and aerospace areas such as satellite attitude control, helicopter, inertial navigation system, astronaut's training device, etc. Traditionally, multi-DOF spherical motion is realized by the combination of several

single-axis actuators. This method has some drawbacks such as backlash and friction existing in the external mechanism, kinematic singularities in the workspace, and lack of dexterity in orientation control. Thus, it is difficult for these multi-DOF actuators to achieve high dynamic response and precise motion control. Therefore, the need to develop a spherical actuator that can produce multi-DOF spherical motion in one joint is arising.

The history of multi-DOF actuators can be dated back to the mid-1950s. The first multi-DOF actuator was designed by Williams et al.<sup>1</sup> It has two DOFs motion ability. So far, spherical actuators based on electromagnetic effect, piezoelectric effect, and mechanical methods have been proposed.<sup>2</sup> We focused on the 3-DOF PM spherical actuators here, which have been paid more and more attention recently because of

\* Corresponding author. Tel.: +86 10 82315560.

E-mail address: [whchen@buaa.edu.cn](mailto:whchen@buaa.edu.cn) (W. Chen).

Peer review under responsibility of Editorial Committee of CJA.



Production and hosting by Elsevier

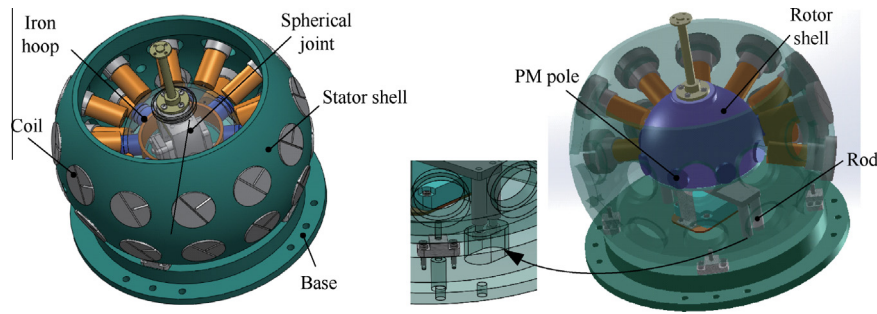


**Fig. 1** CAD model of spherical actuator.

their simplicity in structure, fast response, and compact in design.<sup>3</sup> The PM spherical actuator's applications in industrial and aerospace areas, such as spacecraft attitude control, precision assembling and manufacturing, always require high motion control accuracy.<sup>4</sup> To achieve accurate operation of the spherical actuator, many research works have been done on magnetic field and torque modeling,<sup>2,5–9</sup> orientation measurement,<sup>10,11</sup> dynamic modeling and control algorithm.<sup>3,4,12–14</sup> However, the previous work does not take geometric calibration of the spherical actuator into account. Because of the assembly and fabrication errors, the nominal geometric parameters implemented in the control model will differ from their actual values. 3-DOF rotational motion of the rotor is realized based on the electromagnetic torque generated by the current-carrying coils and PM poles, and position vector errors of the PM poles and coils will affect the torque generation accuracy. In addition, since the rotor is supported by the spherical joint, the geometric errors of the spherical joint will induce the kinematic transformation errors. These errors will result in an inaccurate kinematic and torque model, and thus restrict the control quality and lower the positioning accuracy of the spherical actuator. The geometric calibration has proven to be an effective approach to overcome this problem.<sup>15</sup> Thus, the goal of this paper is to propose a geometric calibration algorithm for the spherical actuator to improve its positioning accuracy.

A number of geometric calibration methods have been studied and utilized to robot manipulators to improve their motion control accuracy.<sup>16–18</sup> Liu et al.<sup>17</sup> analyzed the calibration of a neurosurgical robot system. By compensating the joint axes and transmitting error, the positioning accuracy of this system is successfully improved. Joubair et al.<sup>18</sup> introduced the geometric parameter identification of a XY-Theta precision table by a simple geometric method. In this work, a two-level geometric calibration method was designed for the PM spherical actuator. At the first level, the kinematic parameter errors in the spherical joint mechanism are identified. The calibration model is formulated based on the differential form of kinematic equation. The second level of calibration is to identify the geometric position errors in the magnetization axes of PM poles and coils axes. The calibration model based on the differential form of the torque model is formulated at this level. Because the simultaneous identification of all the PM poles and coils is difficult and may result in complicated computation, each coil is calibrated separately here. It should be noticed that the spherical joint's calibration should be done first to achieve higher calibration accuracy of the PM poles and coils.

## 2. PM spherical actuator

### 2.1. Mechanical description

**Fig. 1** shows the CAD model of the spherical actuator. It is composed of a rotor installed inside the stator. The stator is fixed on the base. The rotor is supported by the spherical joint. There are four rods on the lower side of the spherical joint, and they are fastened onto the base with nuts. Thus, the spherical joint is connected to the stator through the base. The rotor has eight cylindrical PM poles along its equator, and the stator has 24 coils which are arranged in two layers. These two layer coils are symmetrically arranged about the stator equator, and the coils mounted in the stator are air core, which ensures the linear relation between the current input and torque output. The material of the PM poles is rare-earth, which can provide high magnetic field for the spherical actuator. The orientation of the spherical actuator is measured by the encoder and two-axes tilt sensor, which are fixed in the spherical joint. The input power of this actuator is about 96 W. The specifications of the spherical actuator are listed in [Tables 1 and 2](#).

### 2.2. Working principle

**Fig. 2** shows three-DOF rotational motion of the spherical actuator.<sup>12</sup> Current-carrying coils act like a current controlled

**Table 1** Rotor parameters.

Parameter	Value	
Rotor radius (mm)	56.5	
Thickness of iron hoop (mm)	3	
Cylindrical PM pole	Radius (mm)	10
	Height (mm)	20
	Type	N35UH
Remanence of PM pole (T)	1.21	

**Table 2** Stator parameters.

Parameter		Value
Radius of inner stator shell (mm)		100
Radius of outer stator shell (mm)		117
Cylindrical coil	Radius (mm)	12
	Height (mm)	34
	No. of coil turns	1600
Wire type		AWG27 copper wire

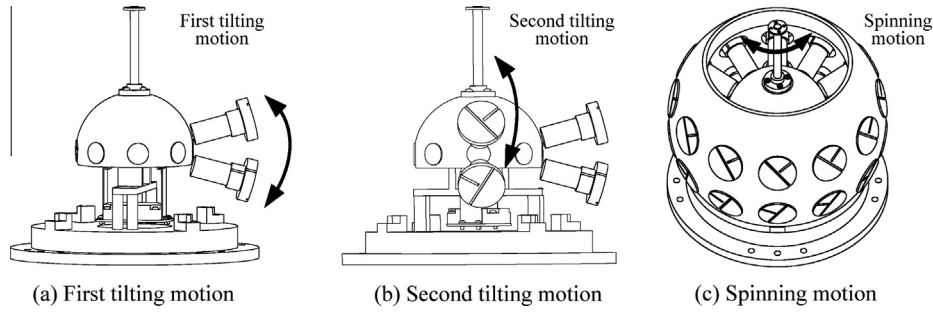


Fig. 2 3-DOF motion of spherical actuator.<sup>12</sup>

magnet and establish a magnetic field around it. The electromagnetic field intensity is proportional to the current magnitude, and the direction depends on the current direction. The rotor motion is realized based on the electromagnetic torques, which is produced by the interaction between current-carrying coils and PM poles. By activating stator coils in longitudinal directions, tilting motion can be created (Fig. 2(a) and (b)). Energizing all the coils in order, spinning motion can be generated (Fig. 2(c)). Thus, by controlling the current inputs of the spherical actuator, any desirable three-DOF rotational motion in the workspace can be realized.

### 3. Calibration of spherical joint

#### 3.1. Kinematic model and error analysis

As shown in Fig. 3, the 3-DOF spherical joint mechanism<sup>19</sup> is comprised of a 1-DOF passive rotary joint in conjunction with a 2-DOF passive universal joint. It can be decomposed into three serially connected 1-DOF revolute joints perpendicular to each other (Fig. 4). The rotation angle of each revolute joint is detected by the sensors installed in the spherical joint. There is a 3-DOF rigid-body rotational motion between the stator and rotor. The three-dimensional transformation matrix from the rotor frame  $F_r$  to the stator frame  $F_s$  is<sup>20</sup>

$$\mathbf{R} = e^{\hat{\omega}_1 q_1} e^{\hat{\omega}_2 q_2} e^{\hat{\omega}_3 q_3}, \hat{\omega}_i = \begin{bmatrix} 0 & -\omega_{i,3} & \omega_{i,2} \\ \omega_{i,3} & 0 & -\omega_{i,1} \\ -\omega_{i,2} & \omega_{i,1} & 0 \end{bmatrix} \quad (1)$$

where  $\omega_1, \omega_2$ , and  $\omega_3$  are three-dimensional unit vectors which represent the direction of three revolute joint axes,  $\hat{\omega}_i \in \text{so}(3)$

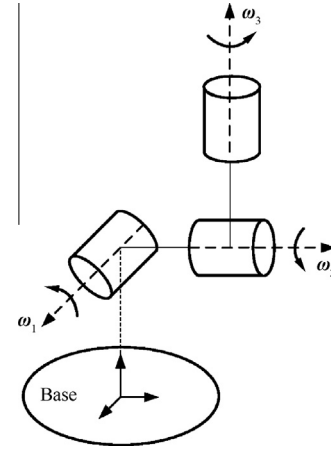


Fig. 4 Kinematic diagram.

is the cross-product matrix of  $\omega_i = [\omega_{i,1} \ \omega_{i,2} \ \omega_{i,3}]^T$ , and  $q_1, q_2$ , and  $q_3$  are the rotation angles of three revolute joints. This transformation matrix  $\mathbf{R}$  provides a unique mapping between the rotor orientation and three revolute joints' rotation angles.

From Eq. (1), we can find that the error sources are the machining and the assembly errors existing in the spherical joint mechanism, which are indicated by the errors in the axes of three decomposed revolute joints ( $\delta\omega_1, \delta\omega_2, \delta\omega_3$ ) and the joint offsets ( $\delta q_1, \delta q_2, \delta q_3$ ). These errors will result in positioning errors directly if nominal values are implemented in the controller. Therefore, the spherical joint calibration is proposed in the following text to solve this problem.

#### 3.2. Spherical joint calibration algorithm

The nominal kinematics model  $\mathbf{R}$  defined by Eq. (1) is a function of  $\omega$  and  $\mathbf{q}$ , where  $\omega = [\omega_1 \ \omega_2 \ \omega_3]^T$ ,  $\mathbf{q} = [q_1 \ q_2 \ q_3]^T$ . Mathematically,

$$\mathbf{R} = f(\omega, \mathbf{q}) \quad (2)$$

By linearizing the kinematic model, the kinematic calibration equation can be given as<sup>21</sup>

$$\delta \mathbf{R} \mathbf{R}^{-1} = \left( \frac{\partial \mathbf{R}}{\partial \omega} \delta \omega + \frac{\partial \mathbf{R}}{\partial \mathbf{q}} \delta \mathbf{q} \right) \mathbf{R}^{-1} \quad (3)$$

where  $\delta \mathbf{R} \mathbf{R}^{-1} \in \text{so}(3)$  denotes the orientation error resulting from the kinematic parameters  $\omega$  and  $\mathbf{q}$ . We express the nominal, calibrated and actual values with the subscript “n”, “c” and “a”, respectively. Then,  $\mathbf{R}_a$  is the actual rotor orientation obtained from the external measurement devices, and  $\mathbf{R}_n$  is the

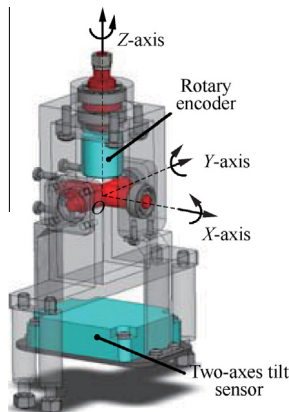


Fig. 3 Spherical joint.<sup>19</sup>

nominal rotor orientation obtained by calculating the Eq. (1).  $\delta \mathbf{R} \mathbf{R}^{-1}$  is also given by

$$\delta \mathbf{R} \mathbf{R}^{-1} = (\mathbf{R}_a - \mathbf{R}_n) \mathbf{R}_n^{-1} = \mathbf{R}_a \mathbf{R}_n^{-1} - \mathbf{I}_3 \quad (4)$$

Eq. (4) can be rewritten as<sup>22</sup>

$$\delta \mathbf{R} \mathbf{R}^{-1} = \ln(\mathbf{R}_a \mathbf{R}_n^{-1}) \quad (5)$$

The objective of the spherical joint calibration is to determine the optimal values of  $\delta \boldsymbol{\omega}$  and  $\delta \mathbf{q}$  based on the measurement data at several rotor orientations which minimize the cost function:

$$\min \left\| \delta \mathbf{R} \mathbf{R}^{-1} - \left( \frac{\partial \mathbf{R}}{\partial \boldsymbol{\omega}} \delta \boldsymbol{\omega} + \frac{\partial \mathbf{R}}{\partial \mathbf{q}} \delta \mathbf{q} \right) \mathbf{R}^{-1} \right\|^2 \quad (6)$$

Eq. (3) is further expressed as

$$\begin{aligned} \delta \mathbf{R} \mathbf{R}^{-1} &= \delta(e^{\hat{\boldsymbol{\omega}}_1 q_1}) e^{-\hat{\boldsymbol{\omega}}_1 q_1} + e^{\hat{\boldsymbol{\omega}}_1 q_1} \delta(e^{\hat{\boldsymbol{\omega}}_2 q_2}) e^{-\hat{\boldsymbol{\omega}}_2 q_2} e^{-\hat{\boldsymbol{\omega}}_1 q_1} \\ &\quad + e^{\hat{\boldsymbol{\omega}}_1 q_1} e^{\hat{\boldsymbol{\omega}}_2 q_2} \delta(e^{\hat{\boldsymbol{\omega}}_3 q_3}) e^{-\hat{\boldsymbol{\omega}}_3 q_3} e^{-\hat{\boldsymbol{\omega}}_2 q_2} e^{-\hat{\boldsymbol{\omega}}_1 q_1} \end{aligned} \quad (7)$$

Substituting Eq. (9) into Eq. (5), we get

$$\begin{aligned} \ln(\mathbf{R}_a \mathbf{R}_n^{-1})^\vee &= \boldsymbol{\omega}_1 \delta q_1 + e^{\hat{\boldsymbol{\omega}}_1 q_1} \boldsymbol{\omega}_2 \delta q_2 + e^{\hat{\boldsymbol{\omega}}_1 q_1} e^{\hat{\boldsymbol{\omega}}_2 q_2} \boldsymbol{\omega}_3 \delta q_3 + q_1 \\ &\quad \times \int_0^1 e^{\hat{\boldsymbol{\omega}}_1 q_1 s} ds \delta \boldsymbol{\omega}_1 + q_2 e^{\hat{\boldsymbol{\omega}}_1 q_1} \int_0^1 e^{\hat{\boldsymbol{\omega}}_2 q_2 s} ds \delta \boldsymbol{\omega}_2 \\ &\quad + q_3 e^{\hat{\boldsymbol{\omega}}_1 q_1} e^{\hat{\boldsymbol{\omega}}_2 q_2} \int_0^1 e^{\hat{\boldsymbol{\omega}}_3 q_3 s} ds \delta \boldsymbol{\omega}_3 \end{aligned} \quad (10)$$

Eq. (10) above can be expressed in the following form:

$$\mathbf{y} = \mathbf{J} \mathbf{x} \quad (11)$$

where

$$\mathbf{J} = \begin{bmatrix} \boldsymbol{\omega}_1 & \mathbf{R}_{0,1} \boldsymbol{\omega}_2 & \mathbf{R}_{0,2} \boldsymbol{\omega}_3 & q_1 \int_0^1 e^{\hat{\boldsymbol{\omega}}_1 q_1 s} ds & q_2 \mathbf{R}_{0,1} \int_0^1 e^{\hat{\boldsymbol{\omega}}_2 q_2 s} ds & q_3 \mathbf{R}_{0,2} \int_0^1 e^{\hat{\boldsymbol{\omega}}_3 q_3 s} ds \end{bmatrix}$$

$\delta(e^{\hat{\boldsymbol{\omega}}_i q_i}) e^{-\hat{\boldsymbol{\omega}}_i q_i}$  is expanded as

$$\begin{aligned} \delta(e^{\hat{\boldsymbol{\omega}}_i q_i}) e^{-\hat{\boldsymbol{\omega}}_i q_i} &= \int_0^1 e^{\hat{\boldsymbol{\omega}}_i q_i s} \delta(\hat{\boldsymbol{\omega}}_i q_i) e^{-\hat{\boldsymbol{\omega}}_i q_i s} ds \\ &= q_i \int_0^1 e^{\hat{\boldsymbol{\omega}}_i q_i s} \delta \hat{\boldsymbol{\omega}}_i e^{-\hat{\boldsymbol{\omega}}_i q_i s} ds \\ &\quad + \int_0^1 e^{\hat{\boldsymbol{\omega}}_i q_i s} \hat{\boldsymbol{\omega}}_i \delta q_i e^{-\hat{\boldsymbol{\omega}}_i q_i s} ds \\ &= q_i \left( \int_0^1 e^{\hat{\boldsymbol{\omega}}_i q_i s} \delta(\boldsymbol{\omega}_i) ds \right)^\wedge + \hat{\boldsymbol{\omega}}_i \delta(q_i) \end{aligned} \quad (8)$$

where  $(\cdot)^\wedge$  is a replacement expression of the operator “ $\wedge$ ” defined in Eq. (1). The “ $\vee$ ” operator defines an inverse transformation of “ $\wedge$ ”, which forms a vector in  $\mathbf{R}^3$  out of a given matrix in so (3).

Substituting Eq. (8) into Eq. (7), we get

$$\begin{aligned} (\delta \mathbf{R} \mathbf{R}^{-1})^\vee &= \boldsymbol{\omega}_1 \delta q_1 + e^{\hat{\boldsymbol{\omega}}_1 q_1} \boldsymbol{\omega}_2 \delta q_2 + e^{\hat{\boldsymbol{\omega}}_1 q_1} e^{\hat{\boldsymbol{\omega}}_2 q_2} \boldsymbol{\omega}_3 \delta q_3 + q_1 \\ &\quad \times \int_0^1 e^{\hat{\boldsymbol{\omega}}_1 q_1 s} ds \delta \boldsymbol{\omega}_1 + q_2 e^{\hat{\boldsymbol{\omega}}_1 q_1} \int_0^1 e^{\hat{\boldsymbol{\omega}}_2 q_2 s} ds \delta \boldsymbol{\omega}_2 \\ &\quad + q_3 e^{\hat{\boldsymbol{\omega}}_1 q_1} e^{\hat{\boldsymbol{\omega}}_2 q_2} \int_0^1 e^{\hat{\boldsymbol{\omega}}_3 q_3 s} ds \delta \boldsymbol{\omega}_3 \end{aligned} \quad (9)$$

where

$$\begin{aligned} \int_0^1 e^{\hat{\boldsymbol{\omega}}_i q_i s} ds &= \int_0^1 \left[ \mathbf{I}_3 + \frac{\hat{\boldsymbol{\omega}}_i}{\|\boldsymbol{\omega}_i\|} \sin(\|\boldsymbol{\omega}_i\| q_i s) \right. \\ &\quad \left. + \frac{\hat{\boldsymbol{\omega}}_i^2}{\|\boldsymbol{\omega}_i\|^2} (1 - \cos(\|\boldsymbol{\omega}_i\| q_i s)) \right] ds \\ &= \mathbf{I}_3 - \frac{\hat{\boldsymbol{\omega}}_i}{\|\boldsymbol{\omega}_i\|^2 q_i} (\cos(\|\boldsymbol{\omega}_i\| q_i) - 1) \\ &\quad + \frac{\hat{\boldsymbol{\omega}}_i^2}{\|\boldsymbol{\omega}_i\|^3 q_i} (\|\boldsymbol{\omega}_i\| q_i - (\sin \|\boldsymbol{\omega}_i\| q_i)) \end{aligned}$$

$$\mathbf{x} = [\delta q_1 \quad \delta q_2 \quad \delta q_3 \quad \delta \boldsymbol{\omega}_1 \quad \delta \boldsymbol{\omega}_2 \quad \delta \boldsymbol{\omega}_3]^\top \in \mathbf{R}^{12 \times 1}$$

$$\mathbf{y} = \ln(\mathbf{R}_a \mathbf{R}_n^{-1})^\vee \in \mathbf{R}^{3 \times 1}, \mathbf{R}_{0,i} = e^{\hat{\boldsymbol{\omega}}_1 q_1} e^{\hat{\boldsymbol{\omega}}_2 q_2} \dots e^{\hat{\boldsymbol{\omega}}_i q_i}$$

Generally, we need to measure many different rotor orientations to guarantee the calibration accuracy. Suppose that  $n$  measured orientation data are made. Combining the orientation errors and the Jacobians, we have

$$[\mathbf{y}_1 \quad \mathbf{y}_2 \quad \dots \quad \mathbf{y}_n]^\top = [\mathbf{J}_1 \quad \mathbf{J}_2 \quad \dots \quad \mathbf{J}_n]^\top \mathbf{x} \quad (12)$$

Eq. (12) can be written as

$$\tilde{\mathbf{Y}} = \tilde{\mathbf{J}} \mathbf{x} \quad (13)$$

The least square solution for  $\mathbf{x}$  is

$$\mathbf{x} = (\tilde{\mathbf{J}}^\top \tilde{\mathbf{J}})^{-1} \tilde{\mathbf{J}}^\top \tilde{\mathbf{Y}} \quad (14)$$

Beginning with the nominal geometric parameters,  $\mathbf{x}$  is solved through iterative substitution, and is updated after each step (Fig. 5). If  $\mathbf{K}$  denotes the original geometric parameters, the updated geometric parameter values  $\mathbf{K}'$  can be given as

$$\mathbf{K}' = \mathbf{K} + \mathbf{x} \quad (15)$$

At each step of iteration, the Jacobian matrix  $\tilde{\mathbf{J}}$  is computed by the current geometric parameters. A deviation metric is defined to evaluate the calibration result, which is given as

$$\varepsilon_1 = \frac{1}{n} \sum_{i=1}^n \|\ln(\mathbf{R}_{a,i}^{-1} \mathbf{R}_{c,i})^\vee\| \quad (16)$$

where  $\mathbf{R}_{a,i}$  is the actual rotor orientation of the  $i$ th orientation,  $\mathbf{R}_{c,i}$  is the calibrated rotor orientation,  $\varepsilon_1$  expresses the average deviation existing in the real and calibrated orientations. This iterative procedure ends until  $\varepsilon_1$  approaches a certain limit  $\varepsilon$ . After calibration, the kinematic equation of the spherical actuator becomes

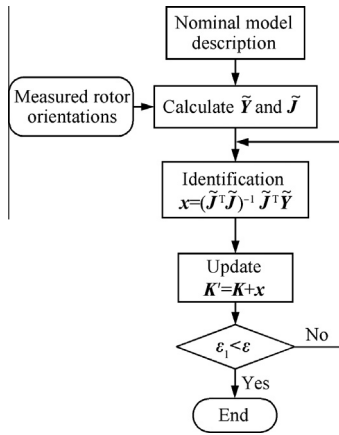


Fig. 5 Calibration process of spherical joint.

$$R_c = \prod_{i=1}^3 e^{(\hat{\omega}_i + \delta \hat{\omega}_{c,i})(q_i + \delta q_{c,i})} \quad (17)$$

### 3.3. Simulation

In this section, simulation studies are conducted on the spherical joint. The kinematic parameters of the spherical actuator are  $\omega_1 = [1 \ 0 \ 0]^T$ ,  $\omega_2 = [0 \ 1 \ 0]^T$ , and  $\omega_3 = [0 \ 0 \ 1]^T$ .

The simulation is conducted according to Fig. 5. Here, it is assumed that no measurement noise exists. Each joint are assigned with kinematic errors as given in Table 3. Based on the definition of revolute joint, the condition  $\|\omega_i + \delta \omega_i\| = 1$  should be satisfied in assigning the errors. The actual rotor orientation is computed by

$$R_a = \prod_{i=1}^3 e^{(\hat{\omega}_i + \delta \hat{\omega}_{a,i})(q_i + \delta q_{a,i})} \quad (18)$$

The number of randomly selected measured orientations is set to five. The identified kinematic errors of joint axes are listed in Table 4, and the joint zero-position errors are shown in Fig. 6. It can be seen that the kinematic errors are fully recovered within three to four iterations. Fig. 7 shows the mean errors  $\epsilon_1$  (defined in Eq. (16)) during the iterative procedure, which is driven from an initial value of 0.051811 to values approximate to zero. The results mean that under the calibrated kinematic parameters description, the actual kinematic transformation matrix can be precisely described, and thus the positioning accuracy can be enhanced.

In consideration of the measurement noise in practical applications, the influence of the measurement noise on the calibration results is studied. The uniformly distributed noise is added to each measurement. Specifically, the measurement result of the rotor orientation is given by

Table 3 Preset kinematic errors.

$i$	$\delta \omega_{a,i}$	$\delta q_{a,i}(\text{rad})$
1	$[-0.00062 \ -0.01570 \ 0.03141]^T$	0.0300
2	$[0.01745 \ -0.00037 \ -0.02094]^T$	0.0250
3	$[0.01571 \ 0.01047 \ -0.00018]^T$	0.0200

Table 4 Identified kinematic errors of joint axes.

No. of iterations	$\delta \omega_{c,1}$	$\delta \omega_{c,2}$	$\delta \omega_{c,3}$
1	$\begin{bmatrix} -0.001146 \\ -0.015610 \\ 0.030657 \end{bmatrix}$	$\begin{bmatrix} 0.016574 \\ -0.000512 \\ -0.023153 \end{bmatrix}$	$\begin{bmatrix} 0.015599 \\ 0.010636 \\ -0.000048 \end{bmatrix}$
2	$\begin{bmatrix} -0.000594 \\ -0.015708 \\ 0.031401 \end{bmatrix}$	$\begin{bmatrix} 0.017521 \\ -0.000347 \\ -0.020914 \end{bmatrix}$	$\begin{bmatrix} 0.015711 \\ 0.010470 \\ -0.000180 \end{bmatrix}$
3	$\begin{bmatrix} -0.000620 \\ -0.015700 \\ 0.031410 \end{bmatrix}$	$\begin{bmatrix} 0.017450 \\ -0.000370 \\ -0.020941 \end{bmatrix}$	$\begin{bmatrix} 0.015710 \\ 0.010470 \\ -0.000180 \end{bmatrix}$
4	$\begin{bmatrix} -0.000620 \\ -0.015700 \\ 0.031410 \end{bmatrix}$	$\begin{bmatrix} 0.017450 \\ -0.000370 \\ -0.020940 \end{bmatrix}$	$\begin{bmatrix} 0.015710 \\ 0.010470 \\ -0.000180 \end{bmatrix}$

$$\tilde{R}_a = R_a e^{\kappa}$$

where  $\kappa = [\delta \tilde{\alpha} \ \delta \tilde{\beta} \ \delta \tilde{\gamma}]^T$  denotes the added noise, which uniformly distributes in the range  $[-0.001, 0.001]$  rad. The simulation results are given in Fig. 8, and the results show that the mean error  $\epsilon_1$  is stable and smaller than the added noise when the number of orientations used for identification is greater than 10. Hence, the proposed kinematic algorithm is robust against the measurement noise.

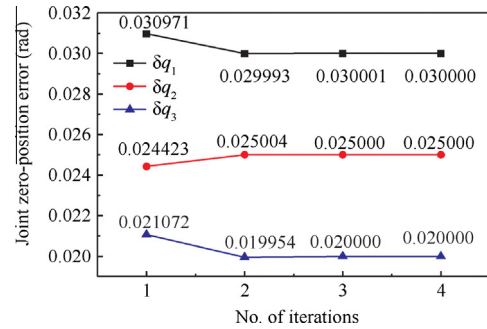


Fig. 6 Identified joint zero-position errors.

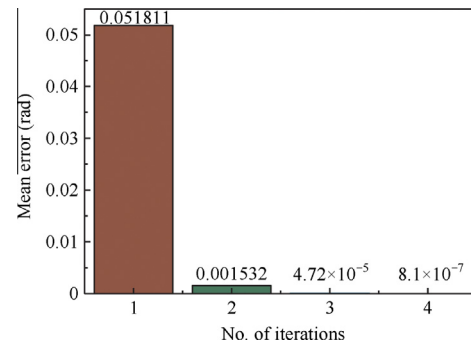


Fig. 7 Mean errors during iterative procedure.



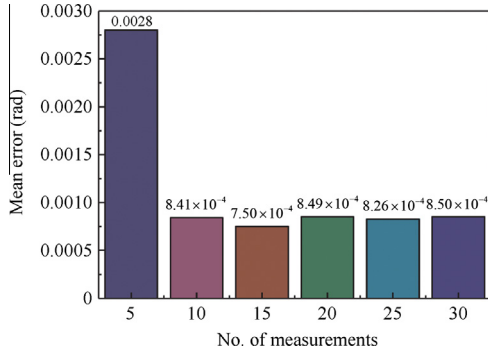


Fig. 8 Mean errors vs number of measurements.

#### 4. Calibration of PM poles and coils

##### 4.1. Torque model and error analysis

The unit vector on the magnetization axes of PM poles in the rotor frame is

$$\mathbf{r}_i^r = \begin{bmatrix} \cos \theta_i \cos \varphi_i \\ \cos \theta_i \sin \varphi_i \\ \sin \theta_i \end{bmatrix} \quad (i = 1, 2, \dots, m) \quad (19)$$

where  $\theta_i$  and  $\varphi_i$  are the polar and azimuth angle of the magnetization axis of the  $i$ th PM pole.

Similarly, the unit vector on the coils axes in the rotor frame is

$$\mathbf{s}_j^r = (\mathbf{R}_c)^{-1} \begin{bmatrix} \cos \eta_j \cos \phi_j \\ \cos \eta_j \sin \phi_j \\ \sin \eta_j \end{bmatrix} \quad (j = 1, 2, \dots, l) \quad (20)$$

where  $\eta_j$  and  $\phi_j$  are the polar and azimuth angle of the  $j$ th coil axis, and  $\mathbf{R}_c$  is the calibrated kinematic transformation matrix from rotor frame to the stator frame.

The torque model is formulated in rotor frame in the previous research,<sup>12</sup> which is given by

$$T = \sum_{i=1}^m \left( \sum_{j=1}^l \tilde{f}(\psi_{ij}) \mathbf{d}_{ij} I_j \right) \quad (21)$$

where  $I_j$  is the  $j$ th coil's current input,  $\mathbf{d}_{ij}$  denotes the direction of the torque element produced by the  $j$ th coil and  $i$ th PM pole, which is given by

$$\mathbf{d}_{ij} = (-1)^{i-1} \frac{\mathbf{r}_i^r \times \mathbf{s}_j^r}{\|\mathbf{r}_i^r \times \mathbf{s}_j^r\|} \quad (22)$$

the positive and negative coefficients of  $\mathbf{d}_{ij}$  are determined by the PM pole's magnetization direction.  $\tilde{f}(\psi_{ij})$  is the torque curve fit function which is given by

$$\tilde{f}(\psi_{ij}) = \sum_{n=0}^6 p_n \psi_{ij}^n \quad (23)$$

where  $\psi_{ij} = \arccos(\mathbf{r}_i^r \cdot \mathbf{s}_j^r)$  is the separation angle between the axes of  $j$ th coil and  $i$ th PM pole, and the calculation results of the coefficients are  $p_0 = -5.40 \times 10^{-3} \text{ N}\cdot\text{m/A}$ ,  $p_1 = 5.18 \times 10^{-2} \text{ N}\cdot\text{m/A}$ ,  $p_2 = -3.73 \times 10^{-6} \text{ N}\cdot\text{m/A}$ ,  $p_3 = -4.2 \times 10^{-4} \text{ N}\cdot\text{m/A}$ ,  $p_4 = 2.39 \times 10^{-5} \text{ N}\cdot\text{m/A}$ ,  $p_5 = -5.07 \times 10^{-7} \text{ N}\cdot\text{m/A}$ ,  $p_6 = 3.78 \times 10^{-9} \text{ N}\cdot\text{m/A}$ .

It can be found from Eq. (21) that there are two error sources influencing the accuracy of the torque model. The first source is the errors in the kinematic transformation matrix, which have been calibrated at the first level of calibration. The second source is the errors in the magnetization axes of PM poles ( $\delta\theta_i$ ,  $\delta\varphi_i$ ) and coils axes ( $\delta\eta_j$ ,  $\delta\phi_j$ ). To ensure the motion control accuracy, these geometric errors should be identified and included in the torque formula. Thus, the second level of calibration is discussed in detail to compensate the position vector errors of PM poles and coils in Section 4.2.

##### 4.2. Calibration model

The nominal spherical actuator's torque model defined by Eq. (21) is an equation of the position vector of the coils axes and PM poles magnetization axes. The calibration model is acquired based on the torque model's differential form, which is given by

$$\delta T = \sum_{i=1}^m \frac{\partial T}{\partial \theta_i} \delta \theta_i + \sum_{i=1}^m \frac{\partial T}{\partial \varphi_i} \delta \varphi_i + \sum_{j=1}^l \frac{\partial T}{\partial \eta_j} \delta \eta_j + \sum_{j=1}^l \frac{\partial T}{\partial \phi_j} \delta \phi_j \quad (24)$$

where  $\delta T$  expresses the torque error in rotor frame which results from the position errors in magnetization axes of PM poles ( $\theta_i$ ,  $\varphi_i$ ) and coils axes ( $\eta_j$ ,  $\phi_j$ ). The partial derivative of the torque function about  $\varphi_i$  is

$$\begin{aligned} \frac{\partial T}{\partial \varphi_i} &= \sum_{j=1}^l \sum_{k=1}^6 \left( \frac{\partial \tilde{f}(\psi_{ij})}{\partial \varphi_i} \mathbf{d}_{ij} I_j + \tilde{f}(\psi_{ij}) \frac{\partial \mathbf{d}_{ij}}{\partial \varphi_i} I_j \right) \\ &= \sum_{j=1}^l \sum_{k=1}^6 \left( \sum_{k=1}^6 k p_k \psi_{ij}^{k-1} \mathbf{d}_{ij} I_j \frac{\partial \psi_{ij}}{\partial \varphi_i} + \sum_{k=0}^6 p_k \psi_{ij}^k I_j \frac{\partial \mathbf{d}_{ij}}{\partial \varphi_i} \right) \end{aligned} \quad (25)$$

The partial derivatives of the torque function about other geometric parameters are similar.

Expressing Eq. (24) in the matrix form as

$$\delta T = \mathbf{A} \delta \mathbf{P} \quad (26)$$

where

$$\delta T = T^u - T^r$$

$$\mathbf{A} = \begin{bmatrix} \frac{\partial T}{\partial \theta_1} & \frac{\partial T}{\partial \theta_2} & \dots & \frac{\partial T}{\partial \theta_m} & \frac{\partial T}{\partial \varphi_1} & \frac{\partial T}{\partial \varphi_2} & \dots & \frac{\partial T}{\partial \varphi_m} & \frac{\partial T}{\partial \eta_1} & \frac{\partial T}{\partial \eta_2} & \dots & \frac{\partial T}{\partial \eta_l} & \frac{\partial T}{\partial \phi_1} & \frac{\partial T}{\partial \phi_2} & \dots & \frac{\partial T}{\partial \phi_l} \end{bmatrix}$$

$$\delta \mathbf{P} = [\delta \theta_1 \quad \delta \theta_2 \quad \dots \quad \delta \theta_m \quad \delta \varphi_1 \quad \delta \varphi_2 \quad \dots \quad \delta \varphi_m \quad \delta \eta_1 \quad \delta \eta_2 \quad \dots \quad \delta \eta_l \quad \delta \phi_1 \quad \delta \phi_2 \quad \dots \quad \delta \phi_l]^T$$

$T^n$  is the nominal torque value, and  $T^a$  the actual (measured) torque obtained from the external measurement device.

The calibration of the coils and PM poles requires comparing the difference between the actual and nominal torque outputs of the spherical actuator. In order to ensure the calibration accuracy, many different rotor orientations are always required to measure. Assuming that we select  $w$  measured torque data, combining the error vectors and the Jacobian matrix into a single equation:

$$\delta \tilde{T} = \tilde{A} \delta P \quad (27)$$

where  $\delta \tilde{T} = [\delta T_1^T \ \delta T_2^T \ \dots \ \delta T_w^T]^T \in \mathbf{R}^{3w \times 1}$ ,  $\tilde{A} = [A_1^T \ A_2^T \ \dots \ A_w^T]^T \in \mathbf{R}^{3w \times (2m+2l)}$ ,  $\delta P$  is solved by the least-squares method:

$$\delta P = (\tilde{A}^T \tilde{A})^{-1} \tilde{A}^T \delta \tilde{T} \quad (28)$$

where  $(\tilde{A}^T \tilde{A})^{-1} \tilde{A}^T$  is the pseudoinverse of  $\tilde{A}$ . In order to evaluate the calibration result, the convergence accuracy is defined mathematically as

$$\varepsilon_2 = \sqrt{\frac{1}{w} (\delta \tilde{T}^T \delta \tilde{T})} \quad (29)$$

where  $\varepsilon_2$  is the average quantified deviation between the measured torques and nominal torques.  $\delta P$  is updated by iterative substitution, and the procedure is repeated until the convergence accuracy  $\varepsilon_2$  is less than the required accuracy  $\varepsilon$ .

The total number of parameter errors that need to be identified is 64. The simultaneous identification of all these parameters is difficult. To solve this problem, each coil is calibrated separately here, which is realized by controlling the current input. Specifically, only one coil is supplied with current input in each calibration cycle. Assuming that only the  $j$ th coil is excited, Eq. (24) is simplified as

$$\delta T = \sum_{i=1}^m \frac{\partial T}{\partial \theta_i} \delta \theta_i + \sum_{i=1}^m \frac{\partial T}{\partial \varphi_i} \delta \varphi_i + \frac{\partial T}{\partial \eta_j} \delta \eta_j + \frac{\partial T}{\partial \phi_j} \delta \phi_j \quad (30)$$

By doing so, the calibration model is greatly simplified. In addition, the identification accuracy is higher and the identification velocity of the error parameters is faster. The total calibration is divided into two situations:

Situation 1: The parameters of eight PM poles and one coil are identified simultaneously. This process needs one calibration cycle.

Situation 2: Each coil is calibrated separately, this process needs 23 calibration cycles.

It should be noticed that the first situation should be conducted first, because only after the calibration of PM poles, can the coils be calibrated separately with sufficient accuracy.

The calibration process of one cycle in two situations is similar, which is given as follows:

- (1) Select  $w_1$  groups of different orientations in the workspace of rotor, and only the  $j$ th coil is excited with current input. Calculate the nominal torque output  $T^n$  and error Jacobian matrix  $A$ . The actual torque is measured at every selected orientation.
- (2) Calculate the bias  $\delta \tilde{T}$  between the actual (measured) torques and the nominal torques.
- (3) Compute the parameter errors  $\delta P$  by Eq. (28).
- (4) The parameters  $P$  are updated by  $P = P + \delta P$ .

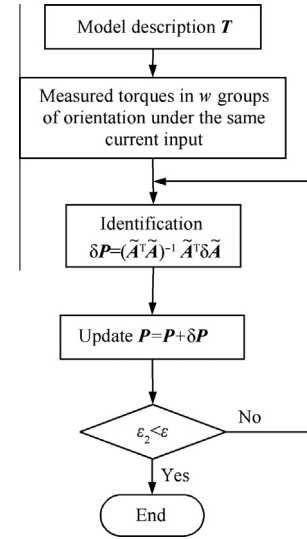


Fig. 9 Calibration process of PM poles and coils.

- (5) As given in Fig. 9, the iterative process starts with the nominal parameters, and is updated with the solution of  $\delta P$  in each iterative process. This process is repeated until the convergence accuracy is satisfied.

#### 4.3. Simulation

Based on the above calibration algorithm, simulation studies are presented to demonstrate the effectiveness and robustness of the proposed algorithm. In the simulation research of the calibration of PM poles and coils, we assume that the spherical joint has been calibrated, and the calibrated value of the kinematic transformation matrix  $R_c$  is given by its nominal value  $R_n$ .

##### 4.3.1. Simulation study on the first situation

The torque generated at 30 orientations is used for identification here, and the current input is set to 2 A. The calibration is based on the interaction between the PM poles and coils. Since only one coil is supplied with current, to ensure that all the PM poles can be identified, the selected orientation set should guarantee that each PM pole can generate force with the excited coil at some orientation.

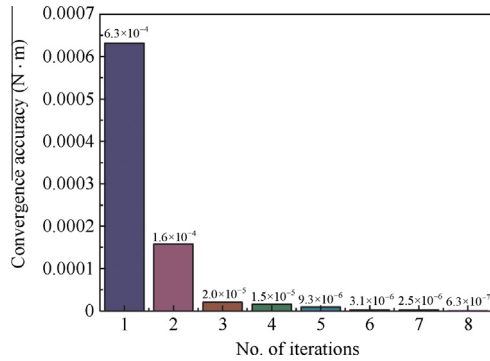
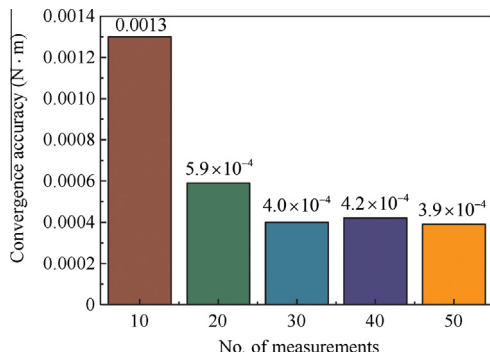
Table 5 shows the nominal, actual parameters and the identified results. The assigned initial position errors can be acquired by comparing the nominal and actual values. We can see that the given errors are fully recovered at the end of the eighth iteration. The simulation results demonstrate the accuracy of the calibration model. Fig. 10 shows the calibration convergence plot with assigned errors, and  $\varepsilon_2$  is driven from an initial value of  $6.3 \times 10^{-4}$  to  $6.3 \times 10^{-7}$  within eight iterations.

To study the effect of measurement noise on the identification results, extensive simulations are carried out. In the simulation, measurement noise uniformly distributed in  $(-0.0005, 0.0005)$  N·m is injected into each measurement, and torques generated at 30 orientations with noise are utilized for identification. The simulation results are presented in Table 5. We can see that the identified values of the parameters are



**Table 5** Nominal, actual and identified parameters.

Parameter	Nominal value (rad)	Actual value (rad)	Identified result (rad)	
			Without noise	With noise
$\theta_1$	0	0.0200	0.0200	0.0197
$\varphi_1$	0	0.0150	0.0150	0.0157
$\theta_2$	0	0.0200	0.0200	0.0197
$\varphi_2$	0.7854	0.8004	0.8004	0.8003
$\theta_3$	0	0.0100	0.0100	0.0105
$\varphi_3$	1.5708	1.5808	1.5808	1.5810
$\theta_4$	0	0.0200	0.0200	0.0204
$\varphi_4$	2.3562	2.3762	2.3762	2.3768
$\theta_5$	0	0.0100	0.0100	0.0095
$\varphi_5$	3.1416	3.1566	3.1566	3.1567
$\theta_6$	0	0.0100	0.0100	0.0097
$\varphi_6$	3.9270	3.9520	3.9520	3.9523
$\theta_7$	0	0.0200	0.0200	0.0195
$\varphi_7$	4.7124	4.7224	4.7224	4.7225
$\theta_8$	0	0.0150	0.0150	0.0151
$\varphi_8$	5.4978	5.5178	5.5178	5.5181
$\eta_1$	0.2618	0.2818	0.2818	0.2815
$\phi_1$	0	0.0200	0.0200	0.0202

**Fig. 10** Calibration convergence.**Fig. 11** Convergence accuracy vs number of measurements.

sufficiently close to the actual values, and the maximum identification error is about 4.7% of the assigned parameter errors. This demonstrates the robustness of the proposed calibration algorithm. Fig. 11 gives the relationship between the convergence accuracy and the number of measurements. It can be found that when the number of measured torques with noise exceeds 20, the convergence accuracy becomes stable.

#### 4.3.2. Simulation study on the second situation

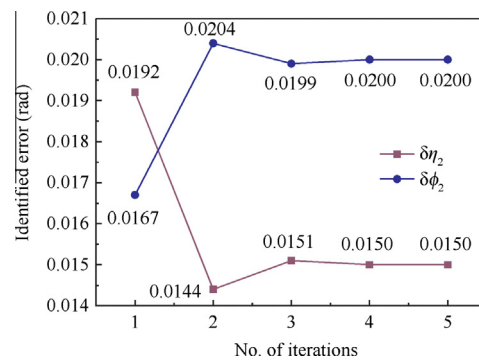
The identification studies on the rest coils are similar. Because the PM poles have been identified before, the calibration cycle of each separate coil is simpler. For a single coil, the theoretical least number of measured torques is one. But it is set to four here for a high accuracy. The selected orientations should ensure that large torque is produced by the coil and the PM poles. The current input is set to 2 A. The initial errors are given by

$$\delta\eta_2 = 0.015, \delta\phi_2 = 0.02$$

The nominal, actual parameters of the coil are

$$\eta_2^n = 0.2618, \phi_2^n = 0.5236, \eta_2^a = 0.2768, \phi_2^a = 0.5436$$

The identified results are shown in Fig. 12. We can see that at the end of the fourth iteration, the preset geometric errors are fully recovered. The calibration's convergence rate in the simulation study of the first situation is slow than that in this simulation example. The relationship between the number of iterations and the convergence accuracy is shown in Fig. 13.  $\varepsilon_2$  is driven from an initial value of 0.0039 to  $3.2 \times 10^{-6}$  within five iterations.

**Fig. 12** Identified errors.

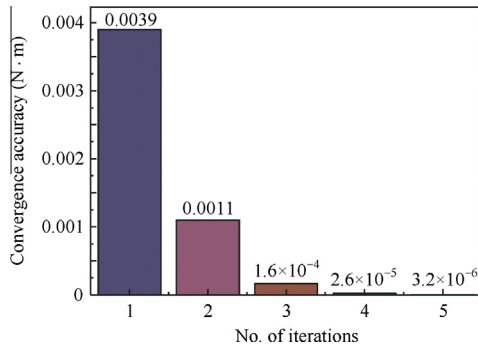


Fig. 13 Convergence accuracy vs number of iterations.

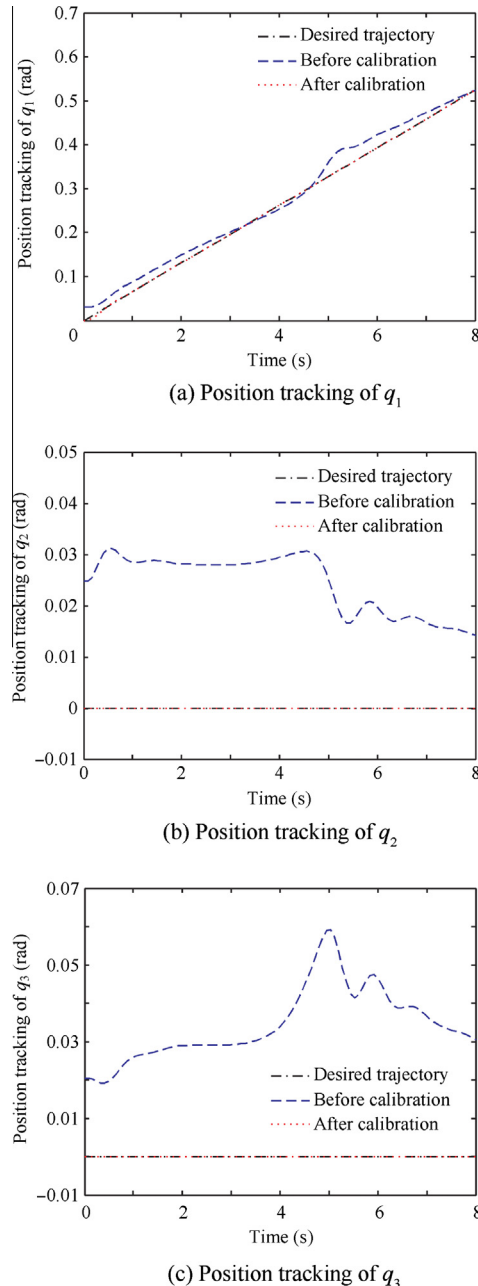


Fig. 14 Simulation results on integrated two-level calibration.

#### 4.3.3. Simulation study on the integrated two-level calibration

In order to verify the effects of the two-level calibration algorithm on the performance of the spherical actuator, a simulation is conducted in MATLAB Simulink. The assigned errors and calibration results of the previous simulation studies on the first and second level are used here. The positioning accuracy of the actuator under the models before and after calibration is compared. In the simulation, the rotor is driven from the initial upright orientation ( $q_1 = 0$  rad,  $q_2 = 0$  rad,  $q_3 = 0$  rad) along the trajectory ( $q_1 = \pi t/48$  rad,  $q_2 = 0$  rad,  $q_3 = 0$  rad) using the computed torque control method, where  $t$  indicates the time.

The simulation results are shown in Fig. 14. The dash-dot line represents the desired trajectory. The dashed and the dotted line indicate the control results by the models before and after calibration, respectively. From the simulation results, we can see that before calibration, there are large movement errors, the maximum steady state tracking error in one decomposed revolution joint is about 0.06 rad. After compensated by the two-level calibration results, the positioning accuracy is greatly enhanced, and the maximum steady state tracking error is nearly zero. The results demonstrate that the proposed two-level calibration method can effectively improve the positioning accuracy of the spherical actuator.

#### 5. Conclusions

- (1) The error sources which affect the kinematic and torque model of the spherical actuator are analyzed.
- (2) The kinematic errors in the spherical joint are calibrated in the first level of calibration, and the results show that the preset kinematic errors in the spherical joint can be fully recovered after calibration.
- (3) The calibration model of PM poles and coils are established in the second level of calibration. The simulation results indicate that the assigned errors in the coils axes and PM poles magnetization axes can be identified, and thus the accuracy of the torque model can be improved.
- (4) The simulation results on the integrated two-level calibration algorithm demonstrate that the positioning accuracy of the actuator can be enhanced after calibration. Since the existing PM spherical actuators have similar structures and working principle, the results presented here can also be applied to other PM spherical actuators.

#### Acknowledgements

This work was co-supported by National Natural Science Foundation of China (No. 50975017), Research Fund for the Doctoral Program of Higher Education of China (No. 20101-102110006), and the Innovation Foundation of BUAA for PhD Graduates.

#### References

1. Williams FC, Laithwaite ER, Eastham JF. Development and design of spherical induction motors. *Proc IEE – Part A: Power Eng* 1959;106(30):471–84.

2. Yan L, Chen IM, Lim CK, Yang GL, Lee KM. *Design, modeling and experiments of 3-DOF electromagnetic spherical actuators*. Dordrecht: Springer Science + Business Media B.V.; 2011.
3. Son H, Lee KM. Open-loop controller design and dynamic characteristics of a spherical wheel actuator. *IEEE Trans Ind Electron* 2010;**57**(10):3475–82.
4. Bai K, Lee KM, Foong S. Direct field-feedback control for multi-dof spherical actuators. In: *IEEE international conference on robotics and automation*; 2011 May 9–13; Shanghai, China. Piscataway: IEEE; 2011. p. 5825–30.
5. Wang QJ, Li Z, Ni YY, Jiang WD. Magnetic field computation of a PM spherical stepper motor using integral equation method. *IEEE Trans Magn* 2006;**42**(4):731–4.
6. Xia CL, Li HF, Shi TN. 3-D magnetic field and torque analysis of a novel Halbach array permanent-magnet spherical motor. *IEEE Trans Magn* 2008;**44**(8):2016–20.
7. Lim CK, Chen IM, Yan L, Yang GL, Lee KM. Electromechanical modeling of a permanent-magnet spherical actuator based on magnetic-dipole-moment principle. *IEEE Trans Ind Electron* 2009;**56**(5):1640–8.
8. Lee KM, Bai K, Lim J. Dipole models for forward/inverse torque computation of a spherical motor. *IEEE/ASME Trans Mechatron* 2009;**14**(1):46–54.
9. Li B, Li GD, Li HF. Magnetic field analysis of 3-DOF permanent magnetic spherical motor using magnetic equivalent circuit method. *IEEE Trans Magn* 2011;**47**(8):2127–33.
10. Lee KM, Zhou D. A real-time optical sensor for simultaneous measurement of three-DOF motions. *IEEE/ASME Trans Mechatron* 2004;**9**(3):499–507.
11. Son H, Lee KM. Two-DOF magnetic orientation sensor using distributed multipole models for spherical wheel motor. *Mechatronics* 2011;**21**(1):156–65.
12. Zhang L, Yan L, Chen WH, Liu JM. Current optimization of 3-DOF permanent magnet spherical motor. In: *IEEE conference on industrial electronics and applications*. 2011 Jun 21–23; Beijing, China. Piscataway: IEEE; 2011. p. 1111–6.
13. Kahlen K, Voss I, Priebe C, de Doncker RW. Torque control of a spherical machine with variable pole pitch. *IEEE Trans Power Electron* 2004;**19**(6):1628–34.
14. Xia CL, Guo C, Shi TN. A neural-network-identifier and fuzzy-controller-based algorithm for dynamic decoupling control of permanent-magnet spherical motor. *IEEE Trans Ind Electron* 2010;**57**(8):2868–78.
15. Abtahi M, Pendar H, Alasty A, Vossoughi GR. Calibration of parallel kinematic machine tools using mobility constraint on the tool center point. *Int J Adv Manuf Technol* 2009;**45**(5–6):531–9.
16. He RB, Zhao YJ, Yang SN, Yang SZ. Kinematic-parameter identification for serial-robot calibration based on POE formula. *IEEE Trans Robot* 2010;**26**(3):411–23.
17. Liu JC, Zhang YR, Li Z. Improving the positioning accuracy of a neurosurgical robot system. *IEEE/ASME Trans Mechatron* 2007;**12**(5):527–33.
18. Joubair A, Slamani M, Bonev IA. A novel XY-Theta precision table and a geometric procedure for its kinematic calibration. *Robot Comput-Integr Manuf* 2012;**28**(1):57–65.
19. Chen WH, Zhang L, Yan L, Liu JM. Design and control of a three degree-of-freedom permanent magnet spherical actuator. *Sens Actuator A: Phys* 2012;**180**:75–86.
20. Murray RM, Li ZX, Sastry SS. *A mathematical introduction to robotic manipulation*. Danvers: CRC Press; 1994. p. 22–31.
21. Chen IM, Yang GL, Tan CT, Yeo SH. Local POE model for robot kinematic calibration. *Mech Mach Theory* 2001;**36**(11–12):1215–39.
22. Okamura K, Park FC. Kinematic calibration using the product of exponentials formula. *Robotica* 1996;**14**(4):415–21.

**Zhang Liang** is a Ph.D. student in the school of Automation Science and Electrical Engineering, Beihang University. His current research interests include actuators, control and automation.

**Chen Weihai** received the B.S. degree from Zhejiang University, China, in 1982, and the M.S. and Ph.D. degrees from Beihang University, China, in 1988 and 1996 respectively. He is currently a professor in the School of Automation Science and Electrical Engineering, Beihang University, China. His current research interests include modular robots, actuators and control.

**Liu Jingmeng** is an associate professor in the School of Automation Science and Electrical Engineering, Beihang University. His current research interests include actuators, precision control, and mechatronics.

**Wu Xingming** is an associate professor in the School of Automation Science and Electrical Engineering, Beihang University. His current research interests include robotics and automation.

**Chen I-Ming** is the director of Intelligent Systems Center in Nanyang Technological University (NTU). Dr. Chen is a Fellow of ASME, and a Fellow of IEEE. His current research interests include wearable sensors, human–robot interaction, and novel actuator design.